Electronic Supplementary Material (ESI) for Energy & Environmental Science.
This journal is © The Royal Society of Chemistry 2019

Probing Microstructure and Electrolyte Concentration Dependent Cell Chemistry via Operando Small Angle Neutron Scattering

Charl J. Jafta*[a], Xiao-Guang Sun[a], Gabriel M. Veith[b], Grethe V. Jensen[c], Shannon M. Mahurin[a], Mariappan P. Paranthaman[a], Sheng Dai[a] and Craig A. Bridges*[a]

[a]Chemical Sciences Division and [b]Materials Science and Technology Division, Oak Ridge National Laboratory, Oak Ridge, Tennessee 37831, United Sates
[c]Center for Neutron Research, National Institute of Standards and Technology, Gaithersburg, Maryland 20899, United States

e-mail: jaftacj@ornl.gov and bridgesca@ornl.gov

Supplemental Information

SANS data collection and analysis

The cell with outer and inner diameters of 28 mm and 18 mm, respectively, and an assembled maximum thickness of 12 mm (see **Fig. S1**) is assembled as shown in **Fig. 1a**, from right to left. The cell contains OMC as working electrode against the TiZr window, a separator (Celgard 3400), an isotopically enriched ^{7}Li metal counter / reference electrode with surface oxidation removed, a ringed stainless-steel spacer and spring (standard for CR2032 coin cells), which all have an outer diameter of 17 mm. Identical cycling experiments (i.e., electrodes, electrolytes, cycling parameters) conducted in standard steel coin cells and in this *operando* SANS cell show the same electrochemical cycling behavior. The isotopically enriched ^{7}Li metal will ensure minimal neutron absorption [1]. The ringed spacer and spring, with an inner diameter of 8 mm, allows for good electrical contact without interfering in the neutron scattering. The polyether ether ketone (PEEK) center, with excellent mechanical and chemical resistant properties, is used to electrically isolate the two TiZr windows and thus the positive and negative electrodes. Before closing the cell, with non-conducting screws, it is filled with the desired electrolyte. This setup allows for background subtraction that will lead to obtaining the scattering predominantly from the OMC electrode. This is done by measuring the scattering from the cell without the OMC electrode, which is used as the background and then subtracted from the fully assembled cell scattering.

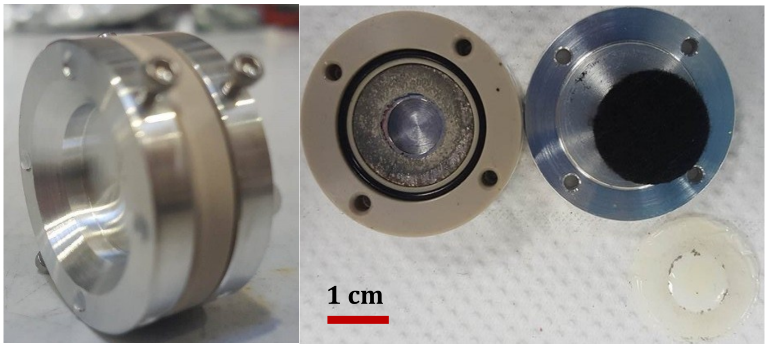

Fig. S1: Pictures of the SANS cell assembled (left) and open (right).

The magnitude of the scattering vector is defined as $q = (4\pi/\lambda)(\sin\theta)$ with λ being the wavelength and 2θ the scattering angle. The data were collected at a single detector configuration in order to maximize the number of measurements per discharge / charge cycle. Specially designed cell holders were 3D printed to place the *operando* SANS cells in the middle of the neutron beam. A Cd aperture of 6 mm was used to ensure scattering from only the middle part of the cell where the OMC electrode is situated, avoiding scattering from the stainless steel. First, *operando* SANS cells were assembled without the OMC electrodes (empty cell) and background measurements were done. The empty cells were transferred to a glovebox wherein they were assembled with the OMC electrodes. The OMC electrodes were left in either 1 M or 4 M electrolyte for 24 hours before assembly. The cells were placed back in the 3D printed holders in the beam and discharged / charged between 0.05 V and 3 V. The constant currents used for the 1 M cell were 50 μA, 100 μA and 150 μA, whereas for the 4 M cell 50 μA and 100 μA were used. The change in current was necessary for time management and is observed at the potential drops in the potentiograms.

The 2D scattering data was reduced to a scattering curve ($\frac{d\Sigma_m}{d\Omega}(q)\ vs.\ q$) by means of the NCNR IGOR software package [2]. The raw data was corrected for transmission, the empty cell scattering was subtracted and then converted to absolute units (cm^{-1}) taking into account the scattering from water. The scattering curves are fitted with a custom model [1, 3]:

$$\frac{d\Sigma_{Tot}}{d\Omega}(q) = \frac{d\Sigma_{frac}}{d\Omega}q^{-p} + \frac{d\Sigma_{DAB}}{d\Omega}\frac{1}{[1+(aq)^2]^2} + G_1\left[\frac{0.398}{s_1}exp\left(-\frac{1}{2}\right)\left(\frac{q-k_1}{s_1}\right)^2\right] + G_2\left[\frac{0.398}{s_2}exp\left(-\frac{1}{2}\right)\left(\frac{q-k_2}{s_2}\right)^2\right] + \frac{d\Sigma_{hq}}{d\Omega}(q) \tag{S1}$$

where the first term obeys the Porod law, the second term is the Debye-Bueche (DAB) function and the third and fourth terms are Gaussian functions to model the Bragg peaks. The last term $\frac{d\Sigma_{hq}}{d\Omega}(q)$ describes the intensity at larger q values and thus the scattering from the micropores, which can be written as [4]:

$$\frac{d\Sigma_{hq}}{d\Omega}(q) = \frac{d\Sigma_{pores}}{d\Omega}(q) + \frac{d\Sigma_{fluct}}{d\Omega}(q) + BG \tag{S2}$$

where the first term is the scattering from the pores and in this case the intensity will scale with contrast. The second term $\frac{d\Sigma_{fluct}}{d\Omega}(q)$ is the fluctuation contribution from lateral imperfections of the carbon layers [4], which is not expected to change during discharge/charge of the cell, and therefore it is constant throughout the experiment. The cell is a closed system with the elemental composition staying constant and therefore the background (BG) will also stay constant.

For the basic principles of SANS related to battery characterization the reader is referred to reference [1]. In brief, the contrast $\Delta\rho^2$, which is directly proportional to the scattering intensity, can be calculated using the following equation:

$$\Delta\rho^2 = [C_{SLD} - Cmp_{SLD}]^2 \tag{S3}$$

Where C_{SLD} is the scattering length density of carbon ($\sim 7 \times 10^{-6} Å^{-2}$) and Cmp_{SLD} is the SLD of the compound causing a contrast with the carbon as shown in equation S3. The contrast is proportional to the SANS intensity measured, i.e. the contrast between C vs Ar (SLD $\sim 0 Å^{-2}$) is $\Delta\rho^2 \approx 49 \times 10^{-12} Å^{-4}$ and that of C vs Li (SLD $\sim -1 \times 10^{-6} Å^{-2}$) is $\Delta\rho^2 \approx 64 \times 10^{-12} Å^{-4}$. This indicates that when Ar is replaced with Li in the carbon pores the SANS intensity will increase by almost a factor 1.5. Similarly, when Li/(PC)$_4$ (SLD $\sim 2 \times 10^{-6} Å^{-2}$) replaces Ar in the pores the contrast ($\Delta\rho^2 \approx 25 \times 10^{-12} Å^{-4}$) and thus the intensity will decrease. **Fig. 1b** shows some of the dominant scattering length density values of the components in the cell and those formed via reduction of the electrolytes. We chose here not to discuss changes in the Porod region due to limitations in the low-q range available during the neutron scattering experiment.

The Bragg peak position is an indication of the pore-pore spacing and the change relative to its starting position is proportional to the strain. Therefore, by following the shift in the peak it is possible to observe the framework expansion and contraction dynamics as a function of discharge / charge [3].

BET of mesoporous carbon

The type-IV N_2 isotherm as seen in **Fig. S2** shows a high adsorption at the low relative pressures ($P/P_0 < 0.1$) after which there is a gradual increase followed by a sharp adsorption increase at $P/P_0 \sim 0.4$. The adsorption at $P/P_0 < 0.1$ is indicative of adsorption in the micropores ($\leq$ 2 nm).[5] The hysteresis in the P/P_0 range of 0.4 – 0.6 can be ascribed to capillary condensation of N_2 molecules in mesopores with relatively uniform dimensions. The pore size distribution calculated by the Barret-Joyner-Halenda (BJH) method using the adsorption data of the isotherm is shown as an inset on the bottom right of **Fig. S2**. The average pore size is calculated to be ~ 4 nm and the BET surface area is determined to be 702 m^2/g. The inset on the top left of **Fig. S2** is a TEM image showing the pore-pore ordering at ~ 10 nm.

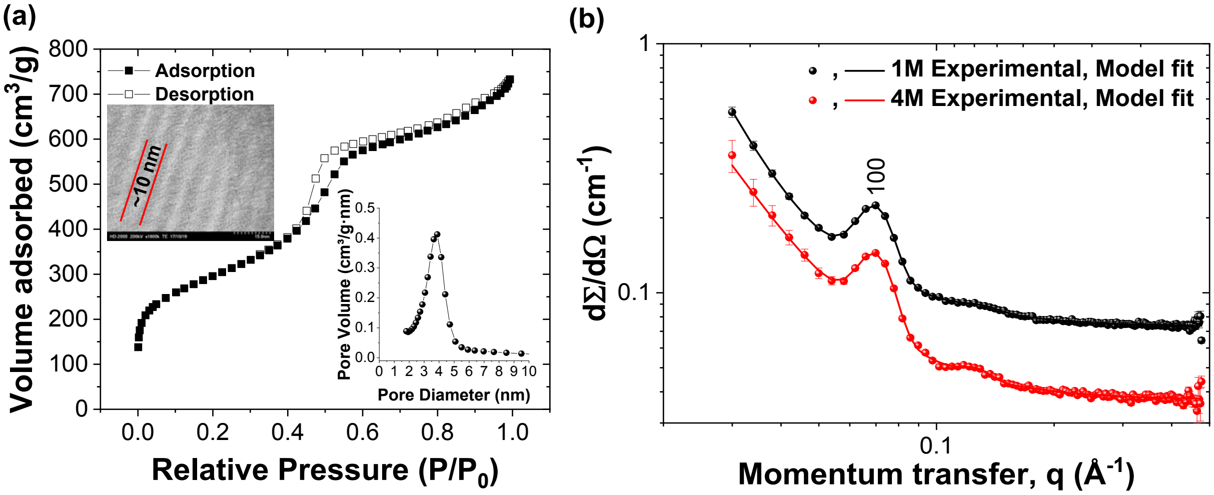

Fig. S2: (a) The N_2 sorption isotherm of the OMC with the pore size distribution as an inset. The inset TEM image indicates the ~10 nm pore-pore ordering, with pores indicated by the lighter regions of ~4 nm diameter. (b) The log-log representation of the scattering curves at OCV for the 1 M LiTFSI/PC (black) and the 4 M LiTFSI/PC (red) electrolyte systems.

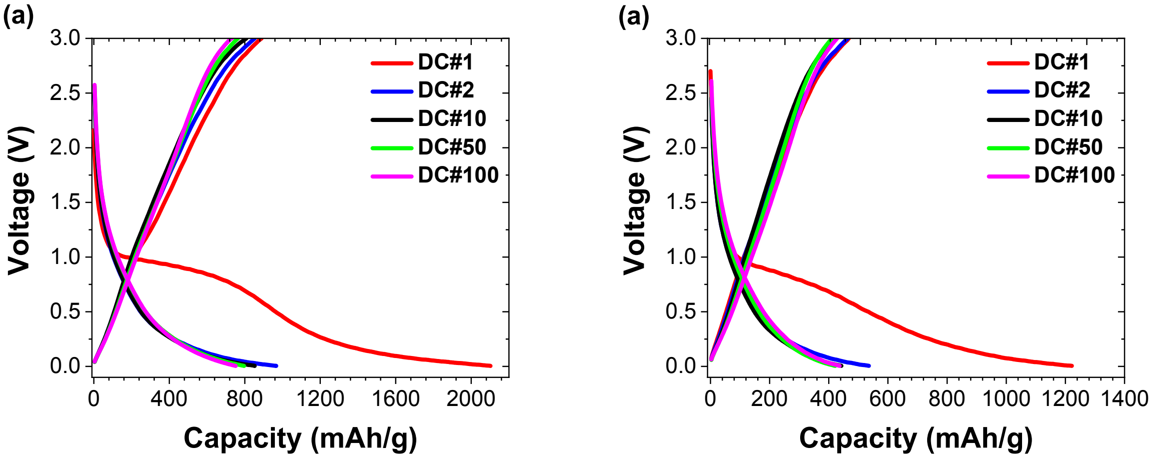

Fig. S3: The potentiograms of the ex-situ cycled cells at a current density of 50 mA/g (~0.13C) for the (a) 1 M and (b) 4 M electrolyte systems. The active material loading for the electrodes used in the *ex-situ* cells were ~ 2 mg/cm^2. An Arbin BT2000 was used for discharging and charging the *ex-situ* cells between 0.005 V and 3.0 V.

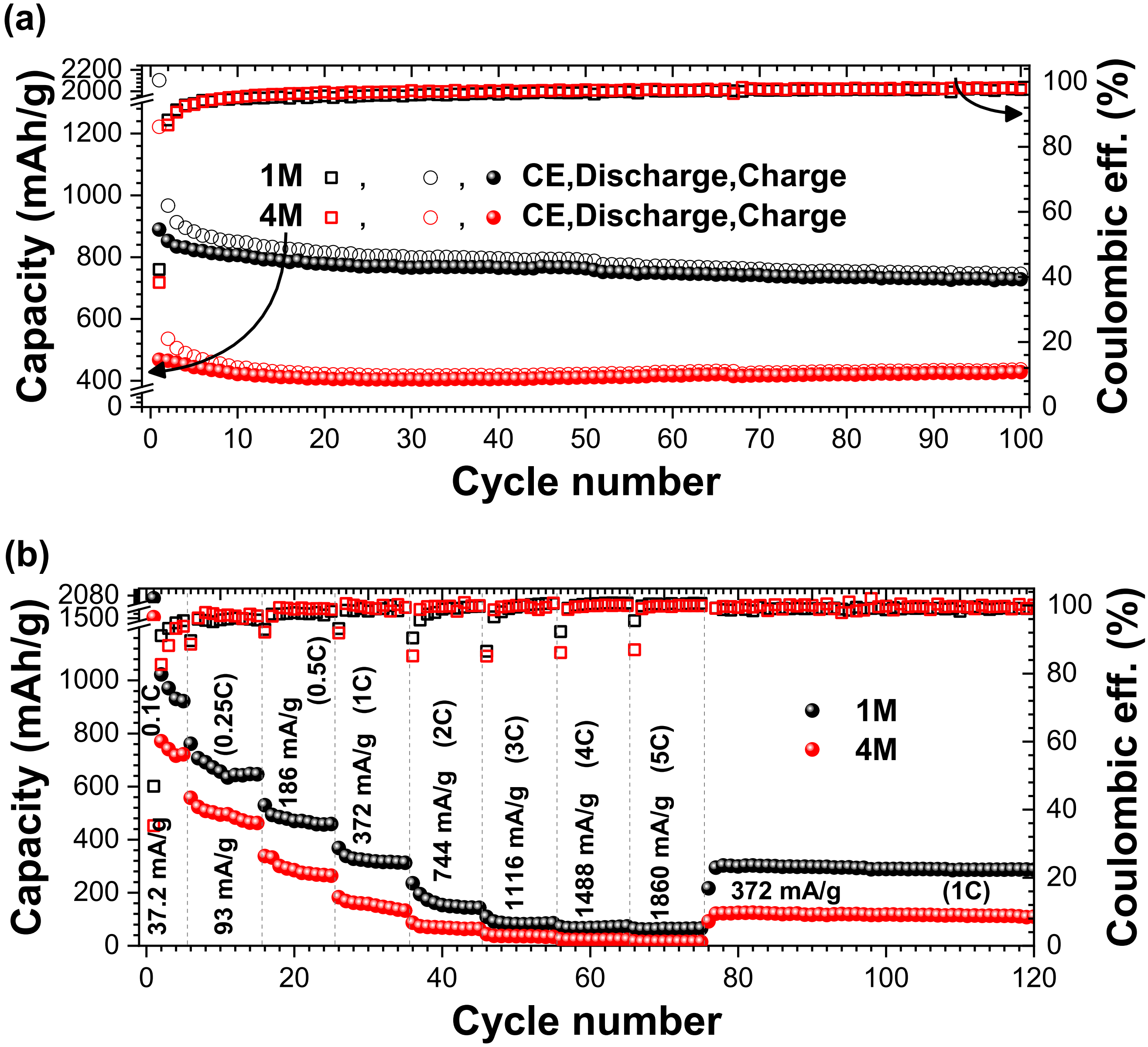

Fig. S4: The *ex-situ* electrochemical data for (a) galvanostatic cycling at 50 mA/g (~0.13C) and (b) rate capability at different current densities. The arrows in (a) indicate the appropriate axis for capacity or coulombic efficiency data.

The cycling performance is similar to previous reports on Li-ion battery charge discharge of ordered mesoporous carbon (OMC) [6].

During the SANS experiment the absolute currents used for the operando discharge were 50 μA, 100 μA and 150 μA as indicated in **Figs. S5a** and **b**. The selection of currents for each cell was based on a compromise between the need to collect data on more than one cycle, and the interest in obtaining high quality data in the initial discharge region where the SEI forms. The currents were therefore initially too low to collect more than one cycle, and were then increased during the first discharge to ensure completion of the data collection during the neutron scattering experiment. The current selection was slightly different for the two cells due to differences in capacity. After the initial discharge, the current densities were held constant at 150 μA and 100 μA for the 1 M and 4 M electrolyte systems, respectively, until the completion of the SANS experiment. The change in the current density, which is small (< 0.5C), should not significantly modify the formation of the SEI as compared to the data collection strategy for the pEIS and XPS.

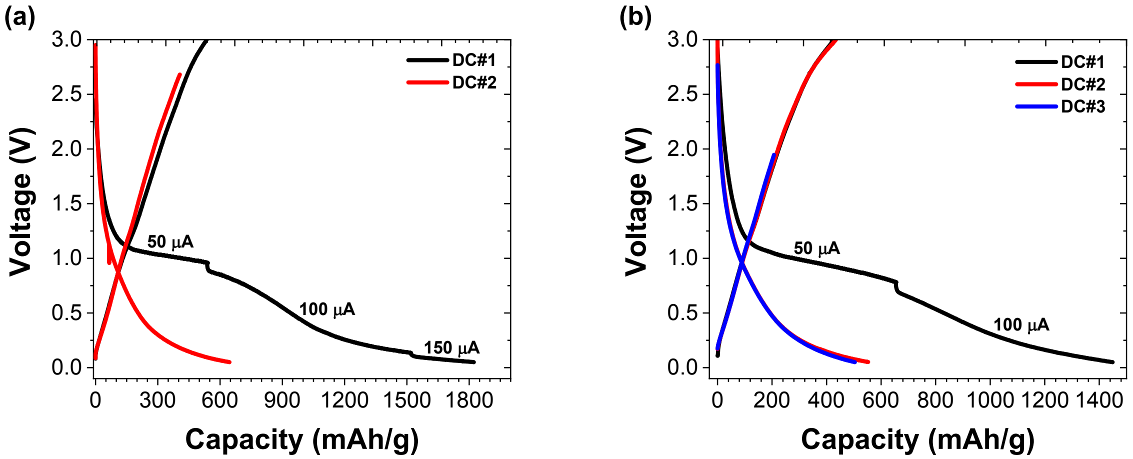

Fig. S5: The potentiograms of the *operando* discharge / charge from (a) the 1 M and (b) 4 M electrolyte systems.

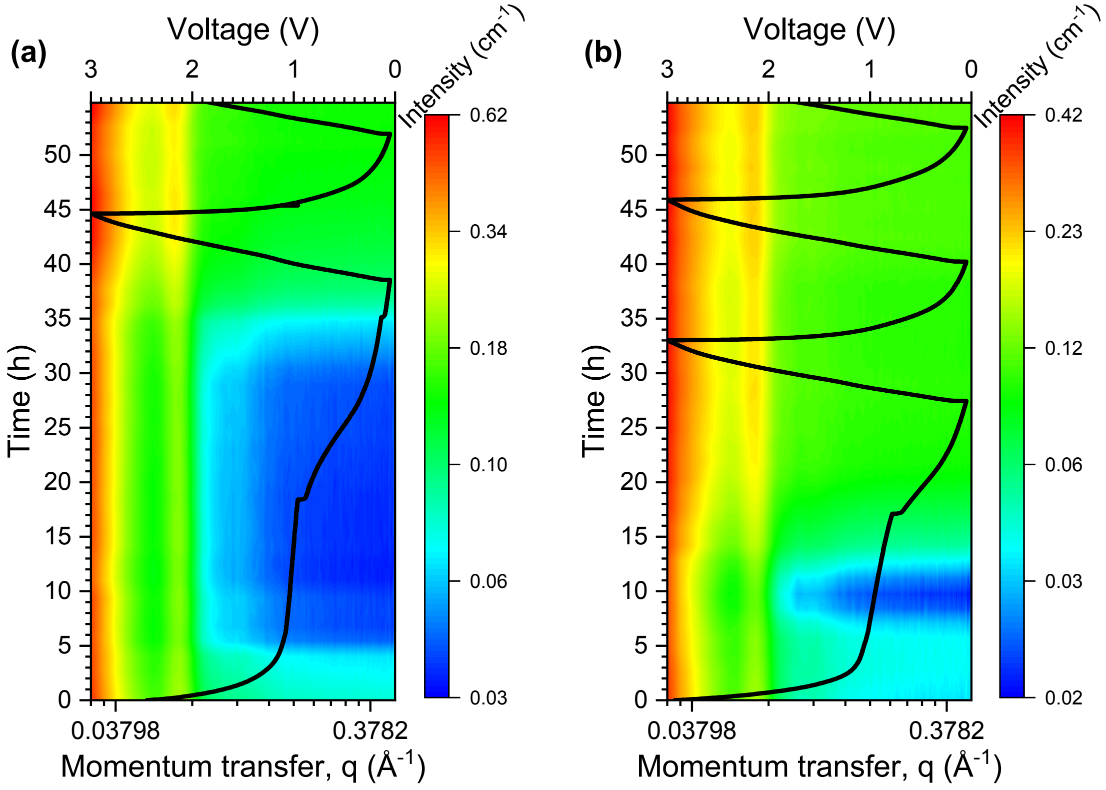

Fig. S6: The SANS scattering intensity (cm^{-1}) as a function of the scattering vector q, discharge / charge time and voltage for (a) the 1 M LiTFSI/PC and (b) the 4 M LiTFSI/PC electrolyte systems.

The *operando* SANS raw data are shown, for the 1 M and 4 M electrolyte systems, in **Fig. S6a** and **b** which include the scattering curves (bottom x-axis in q, Å^{-1}, and z-axis in intensity with absolute units, cm^{-1}) as a function of the potentiograms (top x-axis in voltage and left y-axis in time unit, h). The potentiograms are superposed with the scattering curves showing the scattering intensities at specific potentials during the discharge / charge, evidencing different behavior for the two different salt concentration systems at specific voltages. It is evident that there is a significant decrease in the MPSI ($q > \sim 0.1$ Å^{-1}) earlier in the initial discharge for the 1 M as compared to the 4 M electrolyte system. Also, the MPSI starts to increase much earlier for the 4 M (~0.89 V) as compared to the 1 M (~0.14 V) electrolyte system. During the subsequent charge and discharge cycles there are no significant changes observed from the raw SANS data in this form (**Figs. S6a** and **b**). The peak intensity for the 1 M electrolyte system, in the range~0.05 Å^{-1} < q < 0.08 Å^{-1}, exhibits an initial increase until approximately 16 h, after which it starts to show a decrease until the end of the first discharge. During the subsequent charge, discharge and charge it is apparent that the peak intensity increases during the charge processes and decreases during the discharge process. For the 4 M electrolyte system, the peak intensity shows an initial decrease until approximately 8 h after which it starts to increase again. There are further fluctuations during the subsequent charge and discharge cycles. The *operando* SANS raw data are analyzed by means of the model described in equations S1 and S2, and discussed in detail in the main text. The extracted intensity values reflect the visual evidence, as discussed above for the raw data.

The impedance spectra, for both the 1 M and 4 M electrolyte systems, were fitted with the EEC with the least number of components that gives the best fit, shown as inset in **Fig. S7c**. Similar data treatment is also seen in, for example, ref. [7]. The EEC consists of an ohmic resistance (R_Ω) in series with two parallel components, that consist of a resistance (R_x) and a constant phase element ($R_x||CPE_x$), and a Warburg element (W). The R_Ω is representative of the solution or electrolyte resistance, which can be directly derived from the Nyquist plot where it is equals to the value at $-Z_{imag} = 0$ ($R_\Omega = Z_{real}(-Z_{imag} = 0)$) at high frequency. The process at the higher frequencies is related to the resistances caused by the formation of SEI ($R_{SEI}||CPE_{SEI}$). In the subsequent mid frequencies, the charge transfer resistance is represented by the 2nd parallel component ($R_{ct}||CPE_{ct}$). In the low frequencies region, limited lithium ion diffusion causes virtually a linear increase in the impedance which is represented by the Warburg element. [7, 8] These four components in series are used in the EEC to fit the Nyquist plots from which parameters are extracted for analyses.

We note that a chemical reaction takes place at the Li metal at OCV, forming a passivation layer before the electrochemically driven SEI formation at lower voltage during discharge. This passivation is common after assembly of a battery cell, due to the high reactivity of the Li metal surface [9]. Further study is needed to understand the relationship between electrolyte concentration and passivation of the Li metal surface, to better understand the initial impedance of the battery cell.

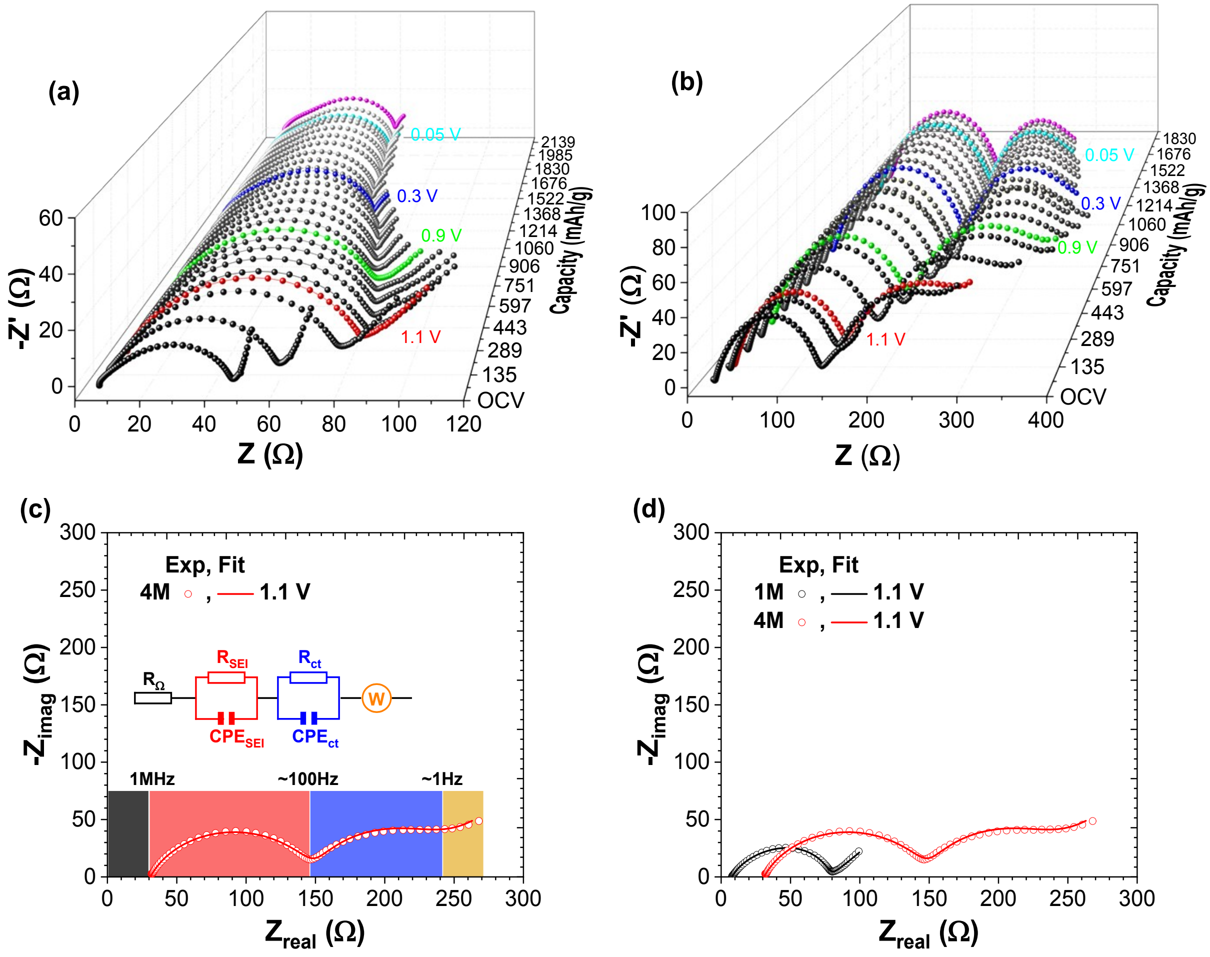

Fig. S7: The Nyquist plots of (a) the 1M electrolyte system and (b) the 4M electrolyte system as a function of the discharge at specific voltages. The Nyquist plot taken at 1.1 V (~175 mAh/g) for the 4M electrolyte system is shown in (c) with the Electrochemical Equivalent Circuit (EEC) as an inset and its fit with the experimental data including the color regions indicating the frequency regions. (d) Examples of the Nyquist plots are shown with their corresponding EEC fits to show the quality of fits used. **Symbols indicate the experimental data, and the line indicates the fit to the data.*

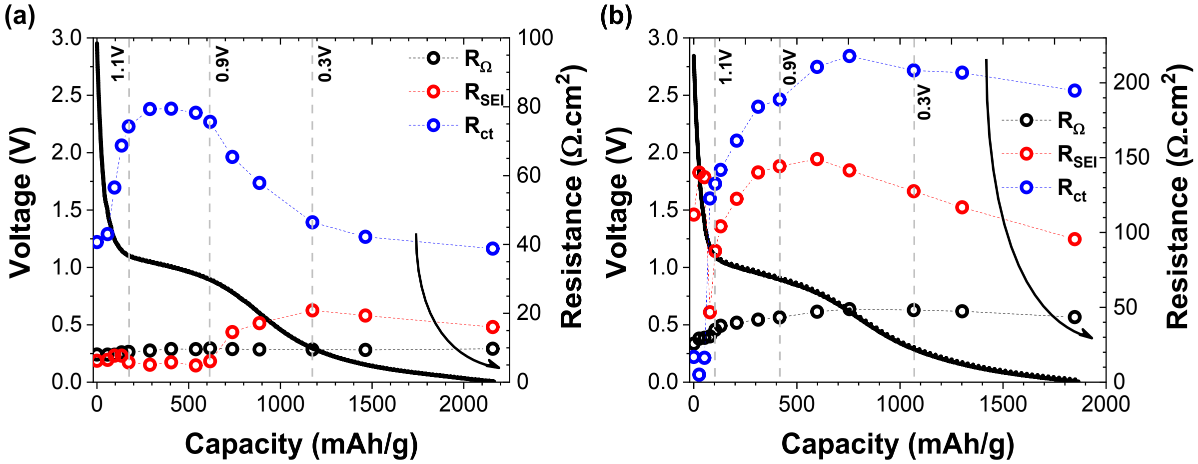

Fig. S8: In-situ EIS data for the (a) 1 M and (b) 4 M electrolyte systems.

Table S1: XPS measured elemental composition from survey scans from the 1 M and 4M electrolyte electrodes

Potential (V)	**Surface elemental composition (at. %)**											
	O		**C**		**Li**		**N**		**F**		**S**	
	1 M	**4 M**	**1 M**	**4 M**	**1 M**	**4 M**	**1 M**	**4 M**	**1 M**	**4 M**	**1 M**	**4 M**
OCV	4.1	4.7	75.4	71.6	6.2	12.3	0.9	2.0	10.7	6.1	2.8	3.2
1.1	6.9	9.3	56.2	59.1	22.3	18.1	0.7	1.7	12.8	7.4	1.1	4.5
0.9	12.5	11.4	47.3	52.2	22.8	21.7	0.8	1.2	12.7	8.4	3.9	5.2
0.3	18.1	15.0	28.1	34.4	35.7	28.0	1.2	2.4	12.0	11.6	5.0	8.6
0.005	15.7	19.0	43.7	32.5	30.2	30.7	1.3	1.1	6.1	8.6	3.1	8.1

Additional information on the cell chemistry observed via XPS and SANS

On the presence of Li_2CO_3

Based on prior studies we may expect a Li_2CO_3 peak located at ~290 eV [10, 11], but as this is conspicuously not present in the C 1s spectra we can claim, at least from the experimental XPS data, that Li_2CO_3 does not form during the initial formation of the SEI during the first discharge. Overall, the presence of Li_2CO_3 is still a subject of debate [10], however there are some key discussions that agree with the current experimental findings. For example, it has been reported that Li_2CO_3 content in the SEI increases with ageing or cycled electrodes [12, 13] and in our case we indeed do not observe Li_2CO_3 during the formation. Also, reports from the group of Edström discussed, from experimental observations, that Li_2CO_3 forms from the reaction of Li_2O with CO_2 and thus samples that do show Li_2CO_3 were not cycled in hermetically sealed holders or were transported to characterization instruments (i.e. XPS) in a manner in which they were exposed to ambient atmosphere [11, 14]. This was also later confirmed by Harilal et al. [15].

Fluorine XPS spectra for LiF

The fluorine XPS spectra deserve further consideration in this voltage range. It should be noted that the LiF peak at binding energy (E_{BE}) values of 56.2 eV (Li 1s) and 685.9 eV (F 1s) in **Figs. 4b** and **c** shift ~0.5 eV to a higher E_{BE} from 0.9 V and 0.3 V for the 1 M and 4 M electrodes, respectively, to 0.005 V. In general, the shift in binding energy can be related to the change in oxidation state of a specific element, but that is not possible in the case of Li nor F. In fact, the four E_{BE} values for measured for LiF (56.1 eV, 56.6 eV, 685.9 eV and 686.5 eV) fall under the umbrella of values reported in literature for the LiF compound as shown in the review by Verma et al. [10] and the references therein. Therefore, a plausible explanation is that the shift is caused by the so-called "electrochemical shift" where a shift in the E_{BE} is observed with electrode potential. This was first discussed in detail by Hansen and D'Agostino [16, 17] where, in brief, the electrostatic potential across the electrochemical interface is shown to influence the electron E_{BE} for a species in the double layer, measured with reference to the Fermi level (E_F) of the substrate. The E_F of the substrate, which is directly proportional to the work function (φ), changes with applied electrode potential. This means that, with a constant photon energy (E_γ) and the kinetic energy (E_{KE}) as measured by the instrument, a change in the applied voltage in the positive direction would result in a change in the E_F or φ in the same direction and vice versa. Therefore, the E_{BE} would shift according to $E_{BE} = E_\gamma - (E_{KE} + \varphi)$. This indicates that LiF is in the Helmholtz layer of both the electrodes from the 1 M and the 4 M electrolyte systems.

Additional XPS spectra

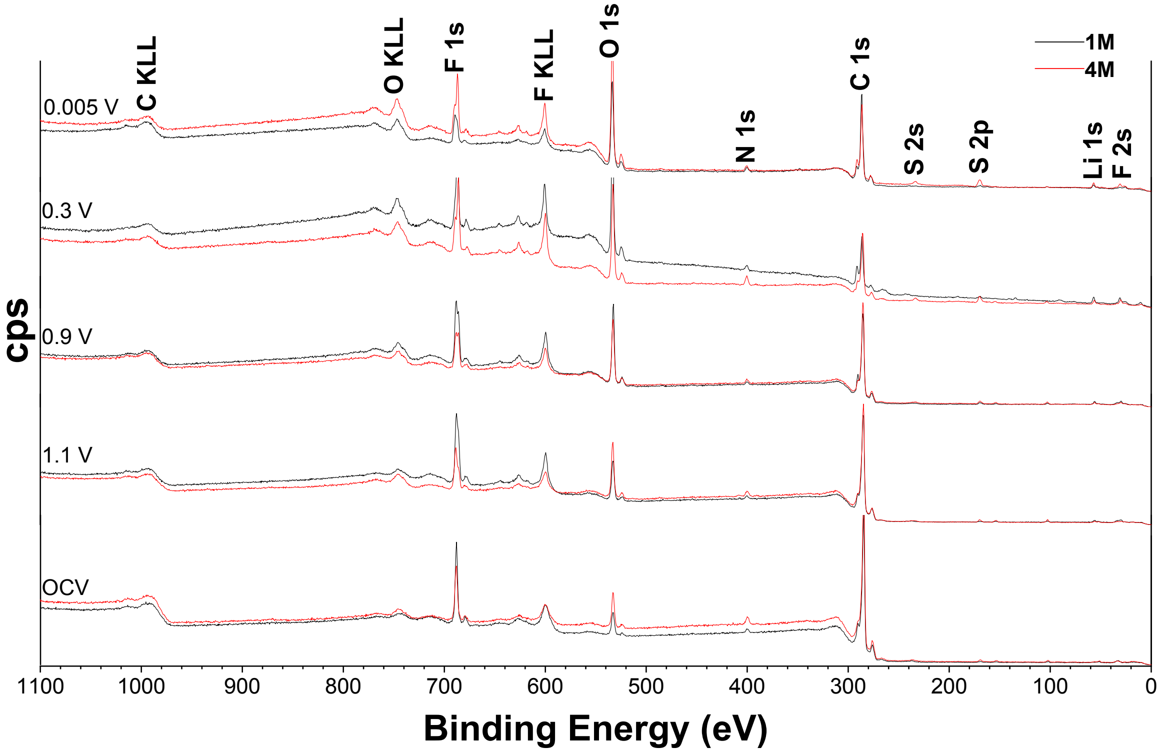

Fig. S8: The XPS survey spectra from the electrodes of the 1 M and 4 M LiTFSI / PC electrolyte cells at OCV, 1.1 V, 0.9 V, 0.3 V and 0.005 V.

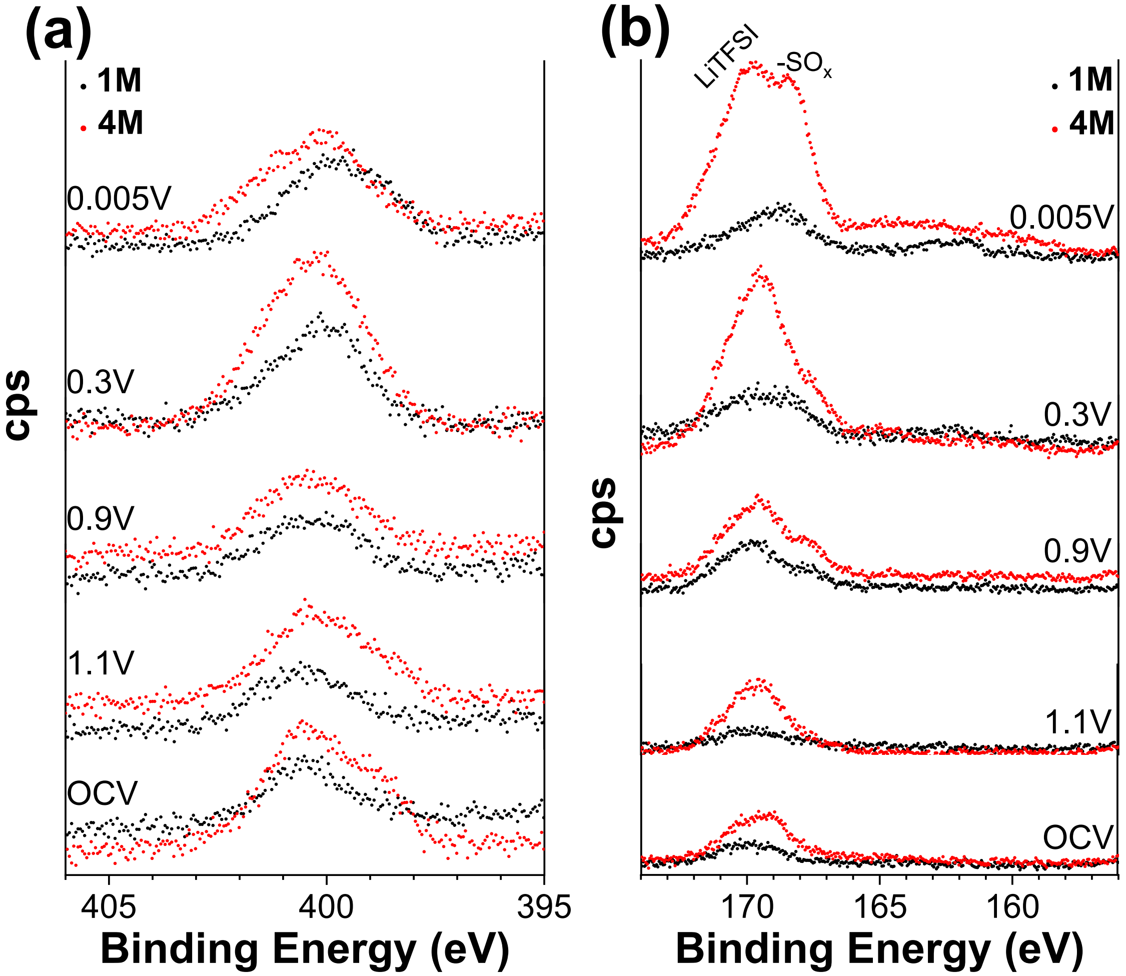

Fig. S9: The XPS spectra of (a) the N 1s and (b) S 2p peaks from the electrodes of the 1 M and 4 M LiTFSI / PC electrolyte cells at OCV, 1.1 V, 0.9 V, 0.3 V and 0.005 V.

The N1s spectra show a main peak at approximately 400.0 eV which is mainly from $LiN(SO_2CF_3)_2$ (LiTFSI), indicating LiTFSI is present in large excess relative to possible degradation products.[18] The S2p spectra shows a main contribution from the peak at 169.6 eV, which is attributed to LiTFSI. The intensity of this peak , from OCV to 0.005 V, is higher for the 4M as compared to the 1M electrolyte system, as may be expected from the higher salt concentration.[19]

References

1. C. A. Bridges, X.-G. Sun, J. Zhao, M. P. Paranthaman and S. Dai, *The Journal of Physical Chemistry C*, 2012, **116**, 7701-7711.
2. S. R. Kline, *Journal of Applied Crystallography*, 2006, **39**, 895-900.
3. C. A. Bridges, X.-G. Sun, B. Guo, W. T. Heller, L. He, M. P. Paranthaman and S. Dai, *ACS Energy Letters*, 2017, **2**, 1698-1704.
4. C. J. Jafta, A. Petzold, S. Risse, D. Clemens, D. Wallacher, G. Goerigk and M. Ballauff, *Carbon*, 2017, **123**, 440-447.

5. S. Storck, H. Bretinger and W. F. Maier, *Applied Catalysis A: General*, 1998, **174**, 137-146.
6. B. Guo, X. Wang, P. F. Fulvio, M. Chi, S. M. Mahurin, X. G. Sun and S. Dai, *Adv Mater*, 2011, **23**, 4661-4666.
7. M. Steinhauer, T. Diemant, C. Heim, R. Jürgen Behm, N. Wagner and K. Andreas Friedrich, *Journal of Applied Electrochemistry*, 2016, **47**, 249-259.
8. J. Illig, M. Ender, A. Weber and E. Ivers-Tiffée, *Journal of Power Sources*, 2015, **282**, 335-347.
9. S. Seki, K. Takei, H. Miyashiro and M. Watanabe, *Journal of The Electrochemical Society*, 2011, **158**, A769 - A774.
10. P. Verma, P. Maire and P. Novák, *Electrochimica Acta*, 2010, **55**, 6332-6341.
11. H. Bryngelsson, M. Stjerndahl, T. Gustafsson and K. Edström, *Journal of Power Sources*, 2007, **174**, 970-975.
12. L. Zhao, I. Watanabe, T. Doi, S. Okada and J.-i. Yamaki, *Journal of Power Sources*, 2006, **161**, 1275-1280.
13. V. Sharova, A. Moretti, T. Diemant, A. Varzi, R. J. Behm and S. Passerini, *Journal of Power Sources*, 2018, **375**, 43-52.
14. K. Edström, M. Herstedt and D. P. Abraham, *Journal of Power Sources*, 2006, **153**, 380-384.
15. S. S. Harilal, J. P. Allain, A. Hassanein, M. R. Hendricks and M. Nieto-Perez, *Applied Surface Science*, 2009, **255**, 8539-8543.
16. W. N. Hansen, *Journal of Electroanalytical Chemistry and Interfacial Electrochemistry*, 1983, **150**, 133-140.
17. A. T. D'Agostino and W. N. Hansen, *Surface Science*, 1986, **165**, 268-276.
18. A. Nytén, M. Stjerndahl, H. Rensmo, H. Siegbahn, M. Armand, T. Gustafsson, K. Edström and J. O. Thomas, *J. Mater. Chem.*, 2006, **16**, 3483-3488.
19. D. Ensling, M. Stjerndahl, A. Nytén, T. Gustafsson and J. O. Thomas, *J. Mater. Chem.*, 2009, **19**, 82-88.